IPCF - CNR - IPCF
Tit: Cl: F:
N. 0003922 25/11/2008

IPCF Rapporto Interno N.

HIGH CHARGE, MULTI MeV ELECTRON BUNCHES FROM LASER-PLASMA ACCELERATION AT MODERATE LASER INTENSITY

Authors
L.A. Gizzi*, S. Betti*, C.A. Cecchetti*, A. Gamucci*, A. Giulietti*, D. Giulietti*, P. Koester*, L. Labate*, N. Patak, F. Vittori

Abstract

Bunches of electrons with energy up to several MeV have been produced using femtosecond laser pulses generated by a table-top, compact laser system focused on laminar gaseous target produced by a supersonic gas-jet. The laser-gas interaction was studied using a full range of optical, X-ray and gamma ray techniques. The electron bunches were detected using a phosphor screen and a magnetic spectrometer to investigate angular and spectral properties. Our measurements show production of highly collimated electron bunches with moderate energy spread. Also, an experimental configuration exists in which generation of high-charge electron bunches can be obtained with high reproducibility and MeV energies. This regime should be further investigated in view of its exploitation for applications requiring high average bunch charge and moderate electron energy, including nuclear activation and bio-medical applications.

ILIL, ISTITUTO PER I PROCESSI CHIMICO-FISICI
Area della Ricerca CNR, Via Moruzzi,1 56124 Pisa, Italy - http://ilil.ipcf.cnr.it
* also at INFN, Sez Pisa, L.go Bruno Pontecorvo, 3, 56124 Pisa, Italy
e-mail l.a.gizzi@ipcf.cnr.it

1 Introduction

Laser WakeField Accelerator (LWFA) [1] is one of the most promising techniques for the acceleration of electron bunches that takes advantage of the high electric fields supported in a plasma. In the LWFA the electrons trapped in the plasma wave are accelerated at the phase velocity of the wave that can be very close to the speed of light. Recent experiments [2, 3, 4], and simulations [5, 6, 7] show that quasi-monoenergetic electron bunches can be accelerated from the background electron plasma population up to high (>100 MeV) energies, operating in the so called bubble regime of LWFA. These experiments require a very high laser intensity and typically produce relatively low charge electron bunches.
Recent theoretical works [8] indicate that with a proper choice of laser, plasma, and injection parameters, the acceleration of electron bunches with small energy spread and short bunch length can occur starting from initially large bunch length and energy spread.
By considering that the energy of an accelerated electron bunches can be increased by multiple collinear or non-collinear injections in plasma channels, the stability of the injection and the reduction of energy required for the production of the initial electrons become the key issues of this process. Kaganovich, et al. [9], have recently observed that with a "moderate intense laser beam" (power <10 TW) unexpected off-axis, well directed, quasi-monoenergetic electron bunches can be produced in a laser wakefield regime. These measurements open a new window for the scheme of the non-collinear LWFA in term of power of the laser required.
We have carried out an experiment to investigate this scenario, searching for the minimum conditions required for a compact, moderate laser power system, to achieve acceleration of electron bunches with high charge and acceptable energy spread for a set of applications.

2 The femtosecond laser source

The Ti:Sa system used in this experiment generates a main pulse of 67 fs duration FWHM with peak power exceeding 2 TW, and a second, lower energy probe with a peak power of 0.1 TW, at the repetition rate of 10 Hz. A schematic view of the entire system is shown in Figure 1.

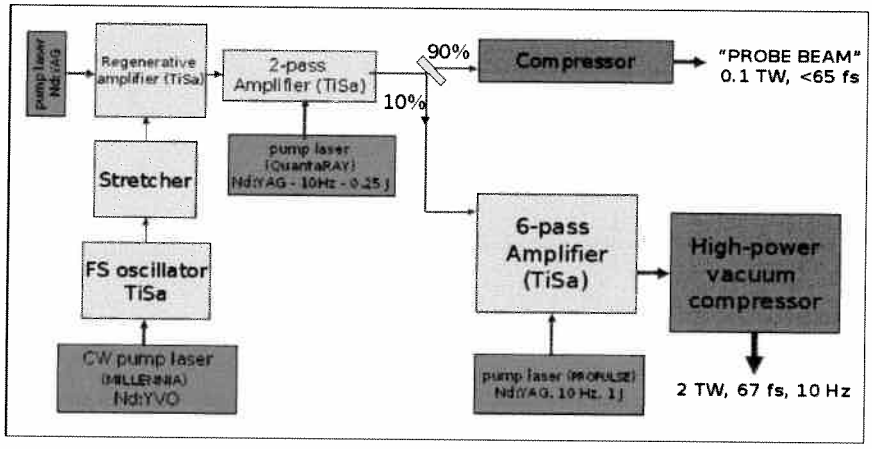

Figure 1: Schematic diagram of the TW, femtosecond laser system. The main beam is transported to the interaction chamber in vacuum.

A Tsunami (Spectra Physics), femtosecond oscillator, pumped by a diode-pumped 5W

Nd:YVO CW laser, generates sub-50 fs pulses at a repetition rate of 82 MHz that are stretched and seeded, at a 10 Hz rep rate, into a regenerative amplifier, pumped by a frequency doubled, Nd:YAG, Q-switched laser. After amplification at the 3 mJ level, the stretched pulses are further amplified by a two-pass amplifier pumped by another, frequency doubled, Nd:YAG, Q-switched laser. The output stretched pulse, containing an energy of approximately 15 mJ, are then split in two pulses containing 90% and 10% of the initial energy respectively. The 90% pulse is expanded to a 7 mm diameter beam and compressed using a single grating (folded) compressor to obtain a final pulse duration of less than 65 fs. The remaining, 10% pulse further amplified by a 6-pass amplifier pumped by a frequency doubled Nd:YAG laser delivering 1J pulses pumping a 2-cm diameter TiSa crystal. The output is further expanded to a 33 mm diameter beam and compressed by a two-grating compressor placed under vacuum. The pulse is compressed to a minimum pulse duration of 67 fs and is then transported under vacuum into the target chamber via two beam steering, motorised turning mirrors, placed in two separate small vacuum chambers. A diagram of the back-end of the laser system, showing a top view of the vacuum compressor and the beam steering mirrors is shown in Figure 2.

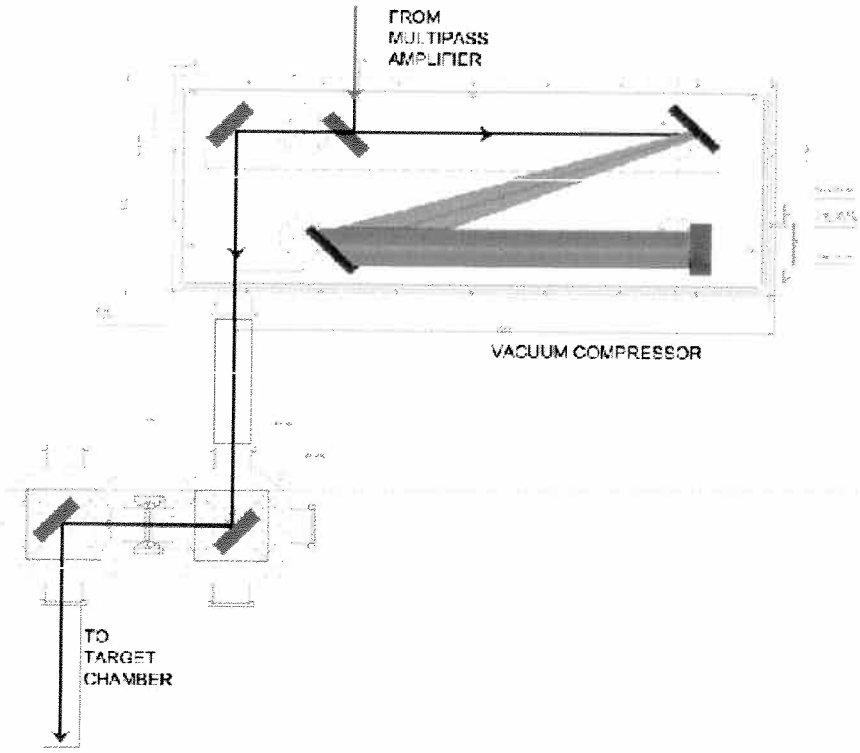

Figure 2: Schematic layout of the last components of the laser system, including the vacuum compressor and the beam steering mirrors.

The temporal and spatial properties of the femtosecond pulses have been characterised in detail using custom developed second-order autocorrelator [10]. The contrast of the laser pulse, i.e. the ratio between the peak power and the low intensity pedestal originating from plepulses and amplified spontaneous emission (ASE) was measured with a third-order cross-correlator (SEQUOIA). In this system, the full power pulse, attenuated by reflections off high quality uncoated glass flats ($\sim 10^2$ attenuation), is split in two equally

intense pulses using a beam splitter. One of the pulses is sent through an optical delay line and is frequency doubled in a BBO crystal. The frequeny doubled pulse is combined with the remaining, fundamental pulse in a non-linear crystal to generate third harmonic radiation. The signal is detected in the forward direction by a photomultiplier.

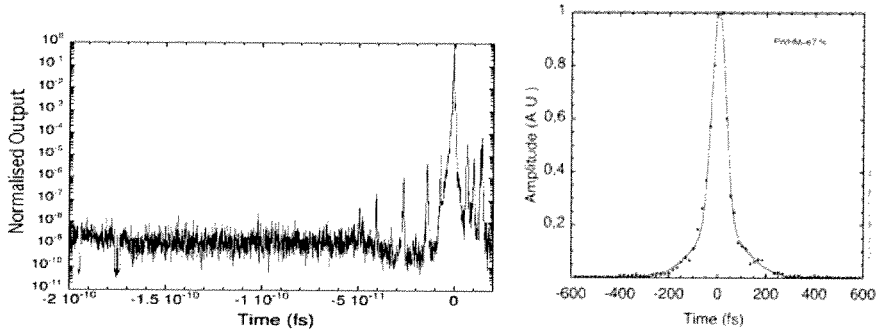

Figure 3: (Left) Cross-correlation curves showing the laser pulse (right) and the detailed structure of the laser pulse in the 200 ps window before the main pulse. (Right) Autocorrelation trace of the laser pulse at full amplification. The trace was fitted with a double Gaussian function to account for the real pulse shape.

The autocorrelation curve obtained from the second-order autocorrelator is shown in Figure 3 (right). The data points fitted with a double Gaussian function, to take into account the low intensity tails of the curve, yield a FWHM of 67 fs. The cross-correlation curve over a range of 200 ps is shown in Figure 3. The plot clearly shows a contrast of 10^9 over the entire explored range. Moreover, the intensity of the short prepulses before the main pulse is below 10^{-5} times the intensity of the main pulse. According to these measurements, our laser system can be considered basically free from pre-pulse.

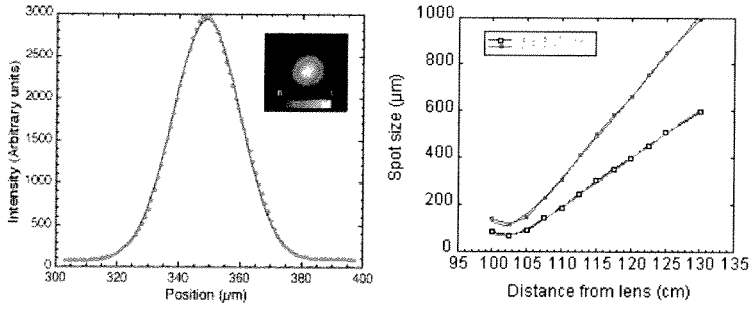

Figure 4: (left) Profile of the beam focal spot (taken along the diameter) of the equivalent plane image of the focal spot (inset) of the laser beam taken at a distance of 7.5 cm before the nominal focal position of a 100 cm focal length. The solid line (blue in the color version), shows the best fit obtained with a Gaussian function. (right) Dependence of the FWHM of the laser beam as retrieved at different distances from a 100 cm nominal focal length lens. A fit with the function for a Gaussian beam is also shown.

The spatial quality of the laser pulse of the low energy probe beam has been studied by means of an equivalent plane monitor (EPM) obtained using a 100 cm nominal focal length optics and a 12 bits CCD camera (a Photometrics Sensys) with a pixel size of 8 μm size. Figure 4 (left) shows an image of the beam taken with the EPM at a distance of 7.5 cm before the best focus of the 100 cm optics. The plot shows a lineout of the beam image

fitted with a Gaussian function. The plot of Figure 4 shows the FWHM of the focused laser spot versus distance, for the 1 meter focal length lens. A fit for this quantity using the function for a Gaussian beam is also shown.
Both the temporal and spatial data show a high quality femtosecond pulse, focusable in a spot size very close to the diffraction limit. According to this result, the FWHM of the pulse best focus for the 100 cm optics is approximately 100 μm.
Scaling this value to the 20 cm focal length off axis parabolic mirror used in our experiment, we can assume a FWHM focal spot of approx. XX μm. Considering the pulselength of 67 fs and an energy of 120 mJ we find that the peak intensity on the targhet can exceed $10^{18} W/cm^2$.

3 The experimental setup

In the experiment both laser beams avalaible from our laser system were used. The laser beam containing the 90% of the front-end energy, CPA2, was used for optical probing purpouses, while the CPA1 laser beam from the 6-pass amplifier, compressed under vacuum, was focused onto the gas-jet target, consisting of He and N2. The gas-jet target was irradiated at full laser energy varying the gas backing pressure (i.e. the pressure into the pipe before the fast valve controlling the nozzle, see fig 5c) to change the value of the maximum density of the neutral gas.

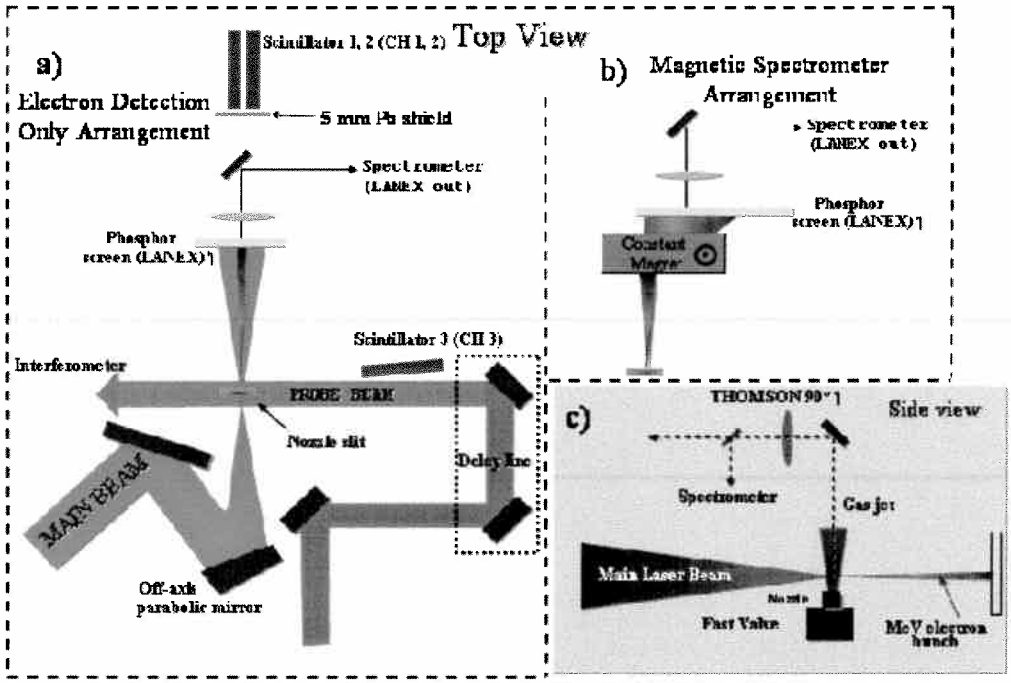

Figure 5: Schematic layout of the experimental setup: a) top view of the experiment in case of LANEX diagnostic without magnetic spectrometer for characterization of the electron bunches (electrons detection configuration). b) particular of the LANEX diagnostic with magnetic spectrometer (electrons characterization configuration). c) Side view of the experimental setup showing Thomson diagnostic arrangement.

Characterisation of the neutral gas was carried out using optical interferometry. The use of two gases He and N_2, enabled us to explore targets characterised by different physical properties mainly related to the atomic number, and, in particular, to the ionization properties under irradiation of ultrashort, intense laser pulses. In figure 6 two picture of the interior of the vacuum-chamber are reported. The nozzle was mounted on a micrometric motorized support in order to move the interaction point along the three cartesian axes (position scan). The off-axis parabolic mirror used to focalize the main beam in a spot of a few micron diameter is also visible. The gas flows out of the rectilinear slit at supersonic speed in order to produce steeper interfaces between gas and vacuum. The vacuum in mantained (pressure of $\sim 10^{-4}/10^{-5}$ Torr) by a turbo-molecular pump (Varian Turbo-V 550) connected to the chamber by a gate-valve.

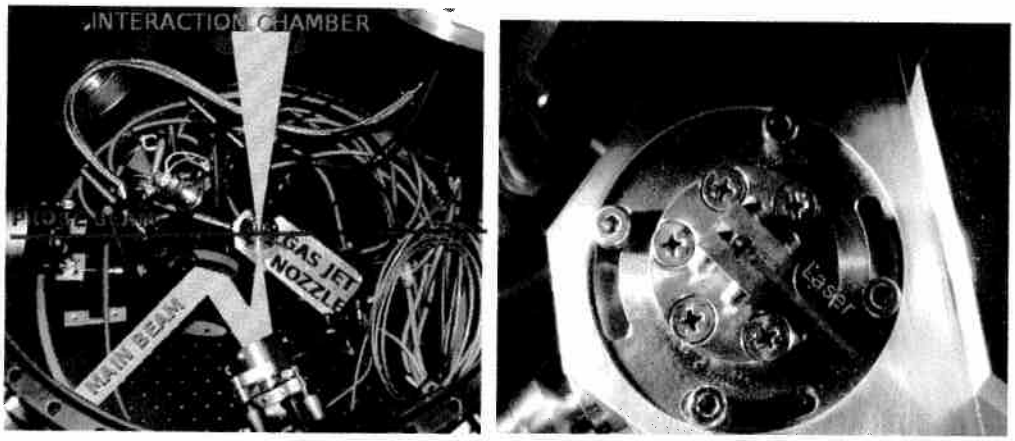

Figure 6: On the left: a picture of the interaction chamber where the main beam and the probe beam propagation axis are drawn. On the right: zoom on the gas-jet target. The nozzle is clearly visible and the direction of propagation of the laser is sketched.

A full scan along the laser porpagation axis and a scan of the position of the focal spot respect to the top of the nozzle have been performed to find the best conditions for acceleration. An important feature consistently observed throughout the experiment is that electron acceleration in our experimental conditions was always found to occur when the focal plane (depth of focus) was located in the proximity of the near edge of the nozzle at ~ 0.6 mm from the top of the nozzle. A full scan in pressure has also been performed, revealing that at higher pressure more stable but less collimated electron bunches are produced.
Several diagnostics were used to study the laser-target interaction and the accelerated electrons. Thomson scattering and Nomarski interferometric were set up perpendicularly to the CPA1 propagation axis to study and characterize its propagation through the gas and the plasma formation via ionization. A second group of diagnostics including scintillators coupled to photomultipliers, phosphor screens (LANEX), permanent magnets and dose sensitive, radiochromich film stacks (SHEEBA), were fully devoted to the detection and characterization of the electron bunches accelerated during the laser-gas interaction.
Figure 5 shows the sketch of the experimental set-up, and the diagnostics used, while in figure 7 a set of the typical output of a single shot is displayed, including an interferogram, the image of the Thomson scattering and the corresponding spectrum and the signal of the three scintillator.

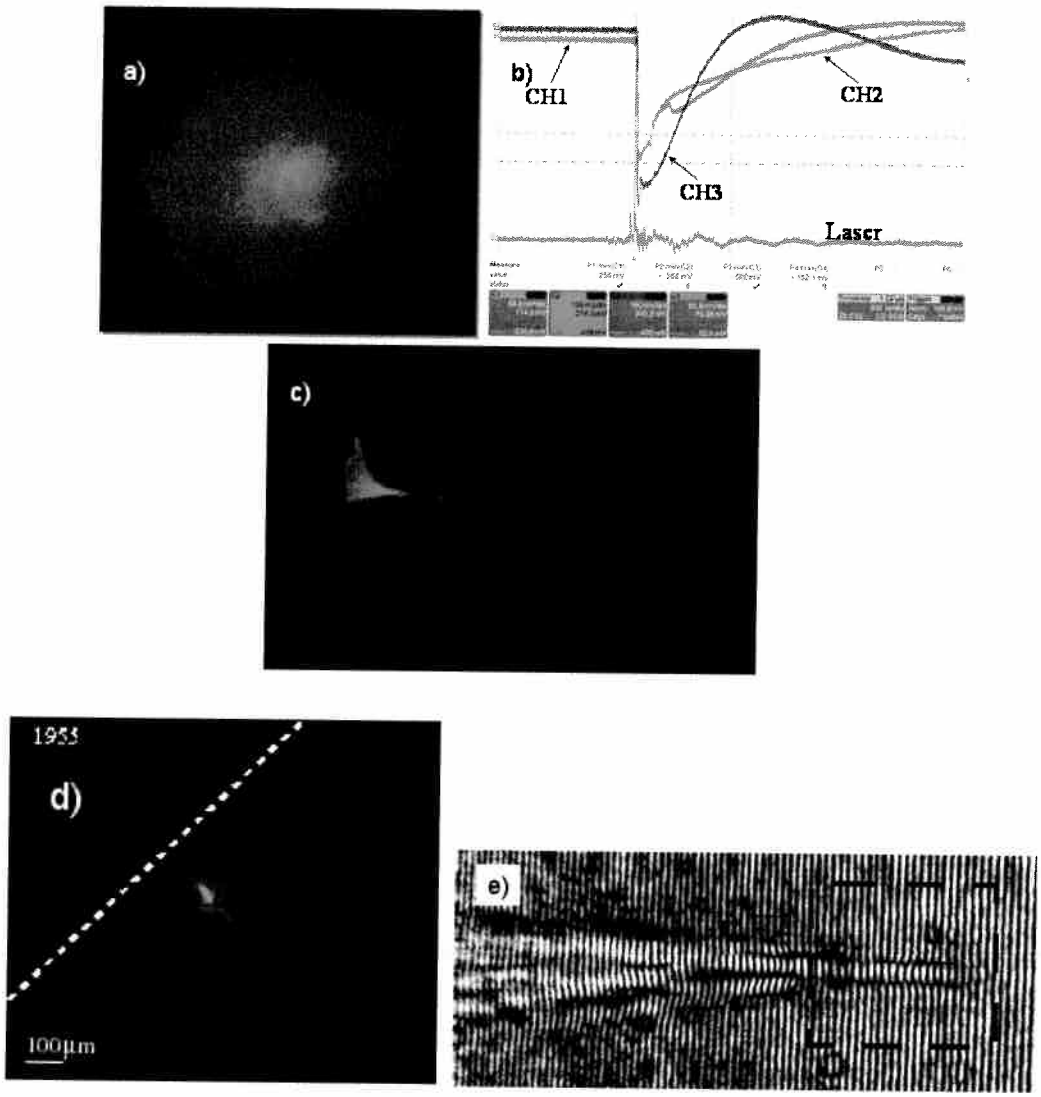

Figure 7: Typical outputs of a single shot: a) image of the LANEX in detection configuration: in this case measurement of the divergence of the electron bunch can be estimated. b) Output signals of the scintillators as labeled in fig.5, and diode signal generated by the CPA1 beam (trigger). c) image of the LANEX in characterization configuration the first magnetic spectrometer used, which had strong border effects and was not suitable for the low energetic part of the electron spectrum. d) Thomson scattering image in case of electron acceleration occurred, the laser propagates from top left corner to the right down one, and the white dotted line represents the long edge of the nozzle. e) Typical interferogram: laser is propagating from left to right, in box is shown the region under analisys. Figure a), b), d), e) belong to the same shot.

4 Optical interferometry

Optical interferometry was employed to retrieve information on the plasma density. The technique is based upon the dependence of the plasma refractive index on the electron density:

$$\eta = \sqrt{1 - \frac{n_e}{n_c}} \backsimeq 1 - \frac{n_e}{2n_c} \tag{1}$$

As a consequence of the above relation a ray of an optical beam passing through a plasma will acquire a phase shift:

$$\Delta\phi = -\frac{2\pi}{\lambda}\int_L [\eta(x,y,z) - 1]\, dx \backsimeq \frac{\pi}{\lambda n_c}\int_L n_e dx \tag{2}$$

with respect to a ray which has travelled the same distance in vacuum. By measuring the phase shift experienced by a laser beam probing the plasma, information about the electron density can therefore be obtained. In fact, it is well known that final expression of the phase shift [11] belongs to a family of integrals called Abel Integrals and for cylindrical symmetry can be inverted analytically to extract the electron density. Interferometry measurements were performed employing a Nomarski modified optical interferometer. The set-up for this arrangement is shown in fig.8.

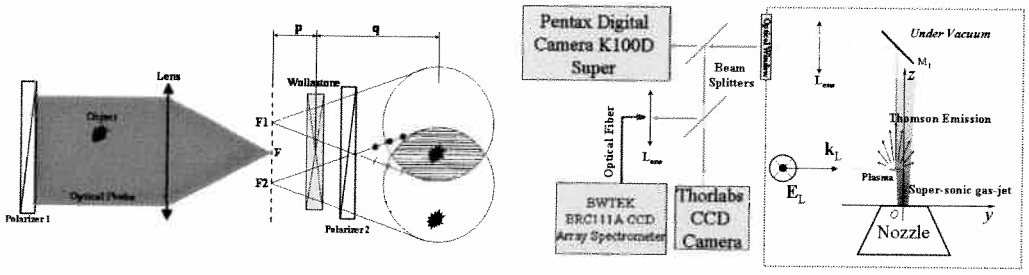

Figure 8: On the left: interferometry experimental arrangement in the Nomarski configuration. On the right: Thomson scattering diagnostic arrangement. The Thorlabs CCD camera was initially used for acquisition, abut in a second phase of the experiment it has been used only for alignment purposes.

The plasma to be probed (phase object) is back-lighted with a low intensity collimated laser beam. The phase object plane is imaged by a lens L onto the detector plane. A Wollaston prism W splits the probe beam into two beams, having relative orthogonal polarization and that appear to be emerging from two separate virtual foci F1 and F2. As a consequence two laser beam spots are projected on the detector, each enclosing an image of the plasma. By appropriately setting the distance between the prism and the detector, the plasma image from one of the spots is made to overlap with an unperturbed region of the other spot. In the overlapping region interference is achieved with the use of a pair of polarizer P1 and P2, which ensure that the two spots have the same polarization and nearly equal intensities. In the typical arrangement, P1 selects a linearly polarized component of the incoming probe beam, while P2 is mounted with the polarization axis rotated by 45 with respect to the axis of P1. An interference pattern is produced with a fringe separation given by:

$$\triangle z = \frac{\lambda p}{\alpha q} \tag{3}$$

where λ is the wavelength of the optical probe, α is the angular aperture of the Wollaston prism, and q and p are the distances between the prism and the detector plane, and

between the Fourier plane of the lens and the prism respectively. The fringe separation can be modified by changing the distance between the focus of the lens and the Wollaston prism. The fringes are usually perpendicular to the separation between the two spots, and their orientation can be changed by suitably rotating the Wollaston prism to optimise spatial resolution along a given direction. During our experiment we have adopted different orientations of the fringed to characterize the profile of the gas-jet.

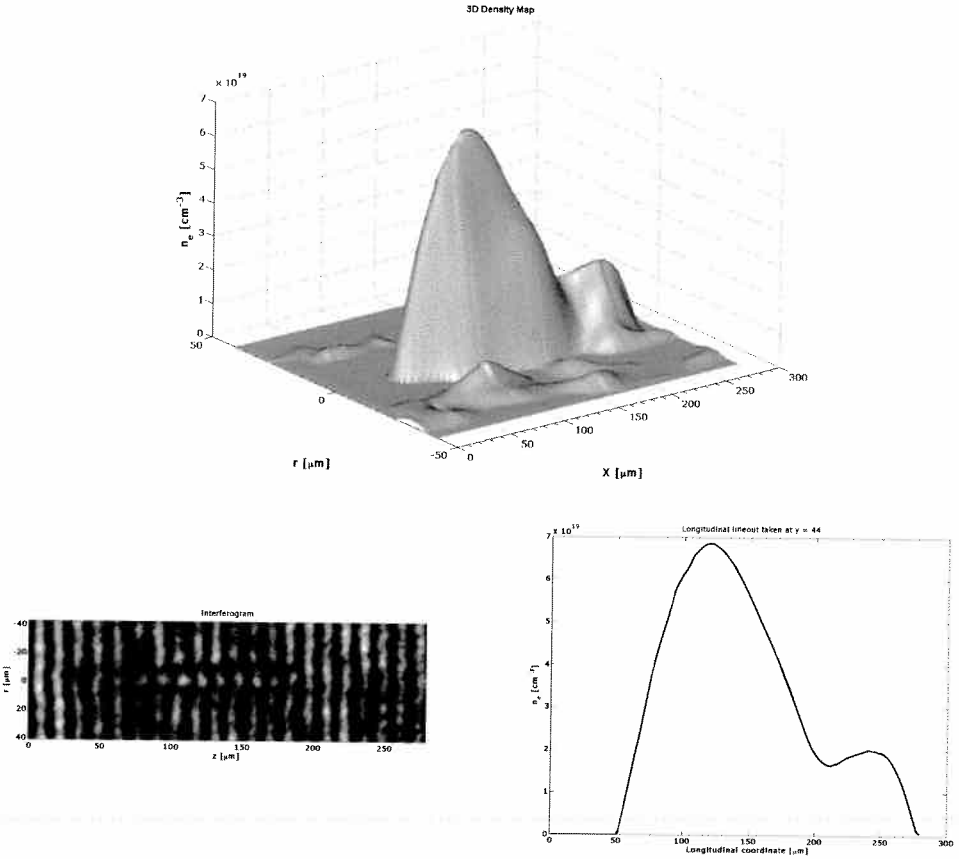

Figure 9: First interferometric result. The shot was performed onto N_2 gas @ 35 bar, with the focal plane 50 μm into the gasjet respect of the edge facing the incoming CPA1, and 400 μm from the nozzle.

Fig. 9 shows the first analysis of an interferogram obtained at the beginning of the laser-gas interaction over a wide temporal range of 65 fs (timing?) for a shot in which the the diagnostics for electrons revealed the electron signal. In fig. 9a) only a region of the whole image is shown. Since the small aperture of our Wollaston in selecting the part of the interferogram to be analyzed it has to be taken into account that one of the two formed images is disturbed by the other one because of the overlapping. The extraction of the electron density from the interferogram has been performed using the code IACRE [12, 13]. The density map thus obtained shows a maximum electron density of $7\,10^{19} cm^{-3}$, and an approximately 200 μm long plasma channel, see fig. 9b), and c). The origin of the second peak in the profile shown in fig. 9c) is still under investigation and may be due to noise in the interferometric fringe pattern.

5 Thomson scattering

Thomson scattering diagnostic reveals the scattering of electromagnetic radiation by a charged particle. In the classical picture of Thomson Scattering, the electrons oscillate in the electric and magnetic components of the of the laser fields and, in turn, they emit radiation. The properties of this scattered radiation are thus related to the properties of the medium.
In case of our laser the main cause of the motion of the electron is due to the electric field component. The particle will move in the direction of the oscillating electric field, resulting in electromagnetic dipole radiation. The scattering can be described in terms of the emission coefficient defined as ϵ where $\epsilon dt dV d\Omega d\lambda$ is the energy scattered by a volume element dV in time dt into solid angle $d\Omega$ between wavelengths λ and $\lambda + d\lambda$.
In our case, with the diagnostic placed perpendicularly to the plane in which the laser field oscillates, the emission coefficient can be written:

$$\epsilon = \frac{\pi\sigma}{2} I n_e \tag{4}$$

where σ is the Thomson differential cross section, n_e is the electron density, and I is the incident flux (i.e. energy/time/area/wavelength).

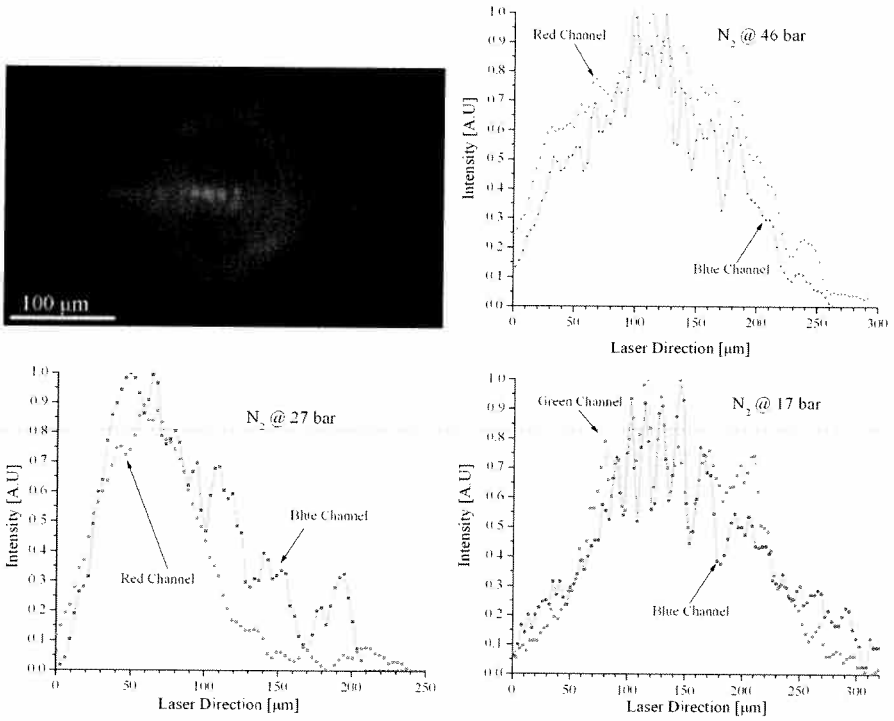

Figure 10: Typical Thomson diagnostic image in RGB color and lineouts of the central channel of 3 shots taken in different pressure conditions as labeled. In the lineout the red, green, and blue lines represent the lineouts of the image when only red, green or blue channel of the RGB color is included. The choice of the channel used depends only by the visibility of the structures.

The Thomson image shown in fig. 10, exhibits an emmision channel $\sim 200\mu m$ long, much consistent with the result from the optica interferometry. Moreover there is a clear spatial modulation in the emission with a periodicity from 14 to 20 μm in the central region,

and in some cases, blue shifted emission up to approximately 500 nm is visible. In some cases, the periodicity was found to depend on the position in the channel. We observe here that the wavelegth associated to a plasma wave excited at an electron density of $1/2n_c r(n_c r = 1.1\,10^{21}\lambda_L \quad [\mu m])$ is $\sim 1.6\ \mu m$. These circumstances are being investigated to identify a possible role of the electron plasma wave in the structure of the emitting region in the Thomson scattering image.

6 Electron beam characterization

Here we focus on the detection and characterization of the laser accelerated electron. For these mesaurements four different diagnostics were used for different purposes. A set of 3 scintillators were set to detect the γ-rays produced by the electrons via bremsstrahlung on the target chamber. A phosphor screen (Kodak LANEX Regular Screen) was placed on the laser axis to image out the accelerated electron beam. The dosimetric film stack (SHEEBA), based upon Radiochromic films[] was used to obtain independent spectro-angular distribution of electrons.
In the case of scintillators, the scattering of energetic electrons within the walls of the chamber generates γ-ray which can be detected and revealed by an oscilloscope. As shown in fig. 5, two scintillator shielded by a 5 mm layer of Pb (CH1 and CH2 in fig. 7(b)), were placed along the laser propagation axis and a third one (CH3 in fig.7(b)), without shielding, was placed perpendicularly to the mentioned direction. The typical output was visualized with a multi-channel oscilloscope, see Fig. 7b). This diagnostic has been used as a basic monitor to find the best conditions for electron acceleration in terms of reproducibility of the signal.
The "LANEX" diagnostic consists of a phosphor screen filtered with a 25 μm Al foil and a optical system imaging its rear surface. When an electron hits the sensitive surface, which faces the gas-jet as shown in fig. 5, the phosphors emit optical (green) radiation from the rear surface of the screen. This radiation is then imaged with a commercial triggerable photocamera (Pentax Digital Camera K 100D Super) with an appropriate focusing objective. This diagnostic, together with the scitillator described above, has been used to detect the electrons accelerated during the laser gas interaction in the so-called electron detection configuration, see fig. 5a). In this scheme the output of the diagnostic enabled the first measurements of the divergence of the electron bunches.

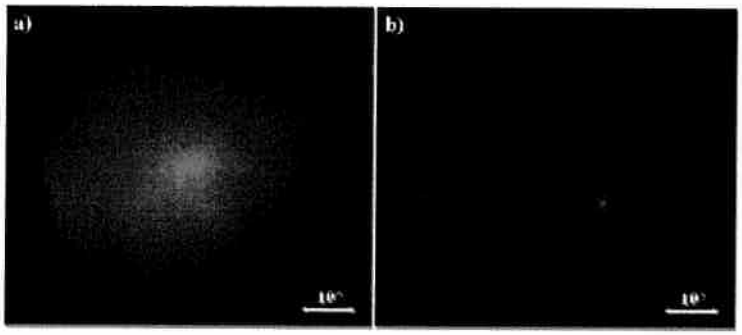

Figure 11: Typical outputs of LANEX in detection configuration. a) non collimated laser-accelerated electrons in case of N_2 gas @ 50 bar. b) collimated laser-accelerated electron bunch in case of He gas @ 50 bar.

Fig. 11 shows the electron beam pattern obtained in two shots. Fig. 11a) presents the typical electron signal from N2 gas (@50 bar backing pressure) that shows a large divergence of approximately 20 degrees. A much narrower angular distribution is found in the case of He gas (@ 50 bar) shown in fig. 11b) which is of the order of 2 degrees, FWHM.

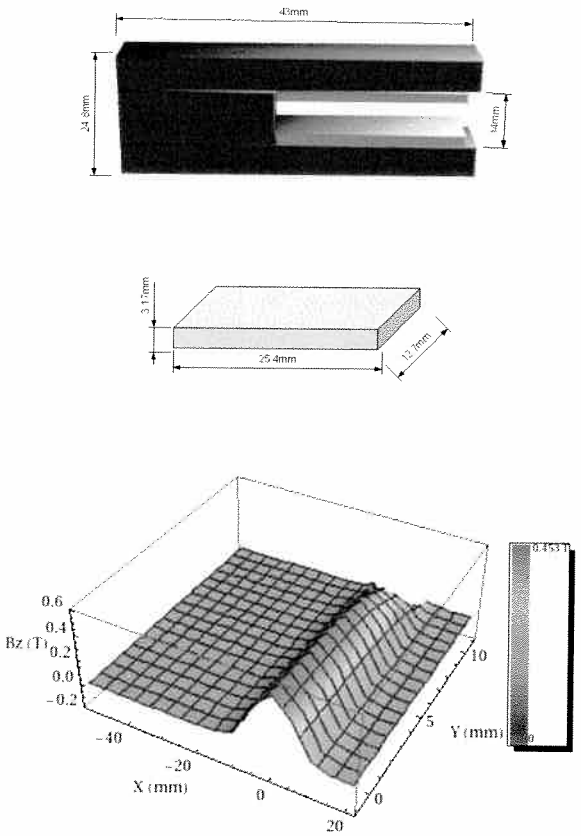

Figure 12: Right:Magnetic field distribution calculated with suitable simulation routine. The zero position represents the ∞-energy for particles and has been set using the position of the laser beam through the slit of the magnetic spectrometer on a white paper placed on the LANEX screen plane. Left: Sketch of our magnetic spectrometer.

A spectral analysis of the accelerated electrons was carried out using a magnetic spectrometer coupled with the LANEX screen. The spectrometer, based upon permanent NeFeB magnets generating a quasi-uniform magnetic field (BMax $\sim$ 0.45 T), was placed at a distance of 44 mm in front of the screen, allowing the study of the energy distribution of the produced electron bunches. Fig. 12 shows the map of the magnetic field amplitude, in the region of interest, in case of the specific geometry used for the spectrometer. A Pb shield with a $\sim$ 0.5 mm slit width was placed in front of the magnet, with the slit direction parallel to the magnetic field, in order to increase the resolution of the spectrometer. A schetch of the magnetic spectrometer with all the relevant dimensions is reported in figure 12.
Electrons propagating through the magnetic field are dispersed under the action of the Lorentz force (relativistic expression) and then hit the LANEX screen in a position dependent on their initial energy and on their initial direction of propagation. In order to take account of the errors introduced by pointing instability and space-charge effects along

propagation, along with the intrinsic resolution of both the imaging acquisition system and the LANEX screen, a suitable algorithm has been implemented (SpecMag, for more explanations see [14]). The most important steps of the algorithm are the simulation of the magnetic field in our particolar arrangement (RADIA tool), the tracing of a set of particles (whose initial properties are generated by a MonteCarlo method) trough the simulated magnetic field by a Runge-Kutta-Fehlberg technic readapted to our needs, the retrieving of the dispersion curve by recording the final position of the simulated electron trajectrories and, finally, the convolution of the dispersion curve with the experimental intensity line-out (previously filtered and dinamically cutted by a subroutine) by another MonteCarlo technic.

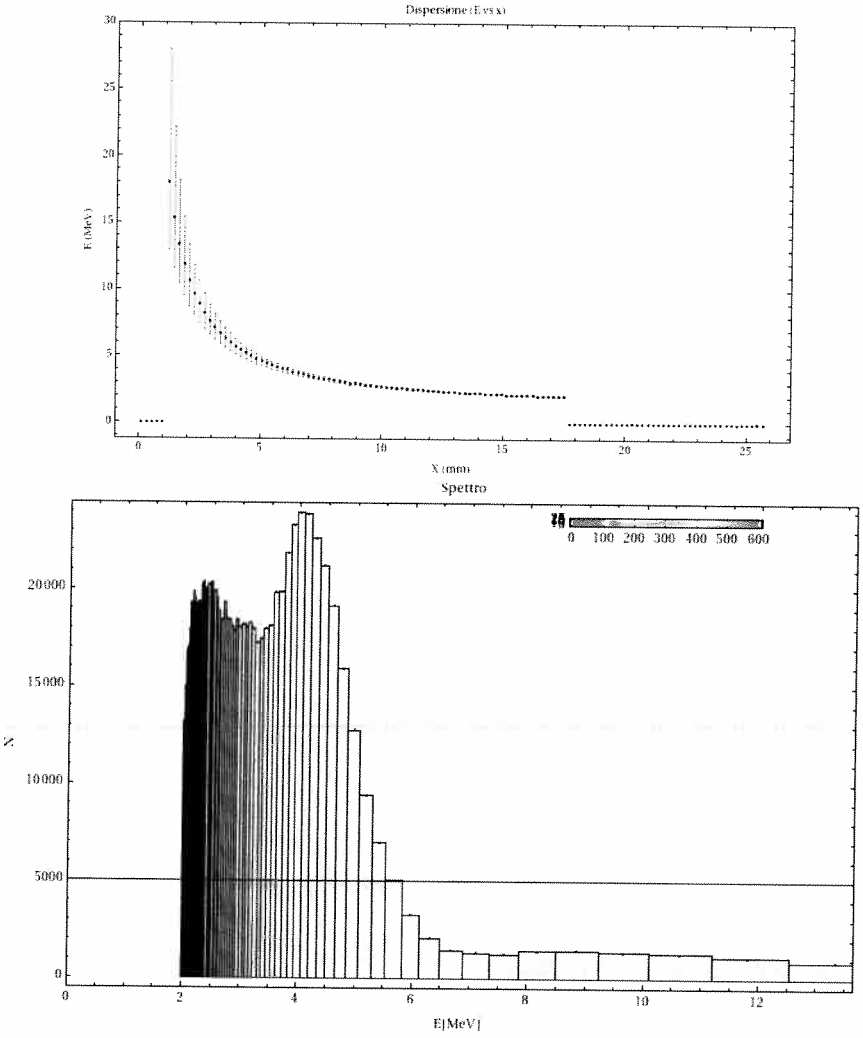

Figure 13: Left: Dispersion curve, i.e. electron position on the detector versus electron energy. Right: on the up-right corner: LANEX image of a tipical dispersion stripe with a clearly distiguishable structure toward high energies. On the main figure the spectrum obtained with the SpecMag algorithm is reported , in which the structure is fully exploited revealing a quasi monoenergetic peak around 5-6 MeV.

The key issue of this procedure is that it permits taking single-shot spectra of electrons with all possible sources of errors (divergence of the beam, pointing instability, finite res-

olution of the acquisition system) incorporated directly in the shape of the spectrum, in a fashion similar to the multi-shot case (this result is obtained by a statistical method). So, in our spectra the error is not reported, having been merged with their shapes.
Another property of the SpecMag algorithm is that it can be adapted to several geometries without relevant changes, allowing future improvements of the system (i.e. the project of a double focusing spectrometer.)
The results obtained by the magnetic spectrometer were confirmed by the measurements carried out using the so-called "SHEEBA" detector which is an energy spectrometer consisting of sandwiched Radiochromic films [78-79] (RCF), HD810 and MD55 in our case. Different types of RCF differ in the thickness of the active gel, and plastic substrates leading to different sensitivities to the action of the ionizing radiation, and dynamic range. The active compound is a micro-crystalline monomer belonging to the diacetylene molecule family, uniformly distributed in a gelatine matrix. Under exposure to ionizing radiation the crystallized diacetylenes undergoes a solid-state polymerization reaction producing a dye polymer referred to as polydiacetylene which results as a change in the Optical Density (OD) in the layer, and it is a localized process. The polymerization begins during the irradiation and does not stop after exposure, but stabilizes to its asymptotic value within 24 hours. Because their sensitive to the ionizing radiation the first layer of SHEEBA is always a thin Aluminium foil which act as a stop filter for optical (scattered laser) and UV radiation and soft X-rays.
The electrons propagate in the detector releasing their anergy till they stop into the medium via several physical mechanisms. In order to take into account these effects and the different materials in the the stack, a Montecarlo code was used [15], which is based upon CERN library GEANT 4.2.0 [16]. The code enabled to model the detailed geometry of the detector, as schematically displayed in Fig 9(a), and to calculate the electron stopping power.

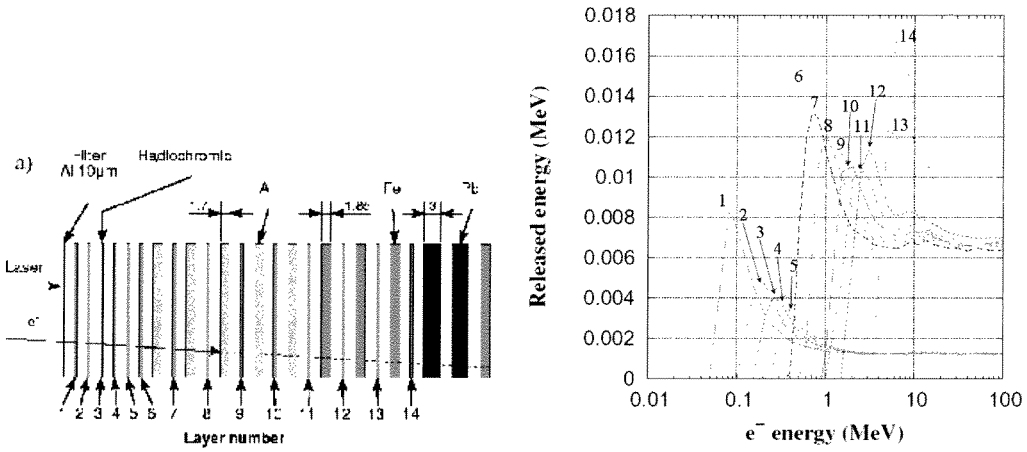

Figure 14: a) SHEEBA set-up: films type, and films distribution. b) Simulation result of the SHEEBA detector response to a single electron: total released energy in the radiochromic film.

The key information of these simulations is the penetration depth of the electrons as a function of their initial kinetic energy. By using this function the electron spectum can be deconvolved considering the position of each layer in the stack [15].
A series of shots have been performed with SHEEBA to confirm the results obtained with the magnetic spectrometer, see fig. 10. The stack used in this case has been set up to

allow four consecutive measurements (form Pos1 to Pos4 in fig. 10) before to remove the detector from the vacuum chamber and verify the results.

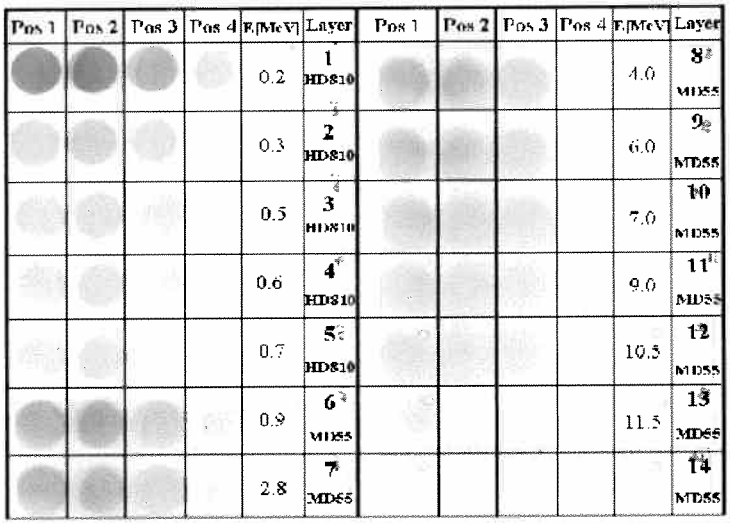

Figure 15: Sheeba output. Columns from Pos1 to Pos4 represent the positions, the column "E" represents the electron energy in MeV, and the last one the layer and type of radiochromic films. In case of Pos1, 2, and 3 a series of 21, 10, and 5 consecutive shots have been taken before to move toward the next position. Position 4 represents one shot only.

7 Conclusions

We reported on an electron acceleration experiment with compact TW system which is preparatory for the 300TW laser facility under construction in Frascati (PlasmonX project [17]). We produced multi-MeV (energy cut-off < 9 MeV) electron bunches with 2TW laser peak-power and we found a condition, laser focus near the front edge of the gas-jet with N-gas and backing pressure of ~ 30 bar, where the electron yield is rather reproducible and where the produced bunches have high charge content (>0.1nC).
High resolved Thomson scattering imaging has been obtained with a triggerable CCD commercial camera coupled with custom electronics allowing to measure structures smaller then 3 μm. With such a diagnostic we directly measured the acceleration length which turns out to be ~ 200 μm. This acceleration length is a direct evidence of some kind of *laser optical guiding*. The mechanisms which provide the guiding can be associated to relativistic *self-focusing* of the laser beam as it propagate through the plasma.
Another important feature of our experiment can be noticed from Thomson imaging system: there is some kind of modulation of the laser pulse at a wavelength about 4 times the plasma wavelength. This modulation may be triggered by relativistic self-focusing. The interaction is now under investigation by means of PIC simulations in order to interpret the acceleration mechanisms and the modulation of the laser intensity.
We wish to point out that all obtained results are fully self-consistent, that is, the electron spectra taken with the Magnetic Spectrometer are in agreement with the SHEEBA results and the Thomson image measurement of acceleration length is roughly equal to the interferometric measures of the length of the plasma density channel.

With this experiment, we have not obtained a new electron's energy record, nor a tiny monoenergetic peak with stable divergence (as it is required by high-energy applications), but our results may be important for applications in several fields, as cancer therapy by mean of *intraoperatory radio-therapy*, thanks to the high charge of our bunches and to low operational costs implied by our experimental configuration.

A Parameters table (to the best of knowledge to date)

Input Parameter		**Output Parameter**	
Laser wavelenght	800nm	Peak electron density	7 $10^{19} cm^{-3}$
Laser pulse duration	$\geq$65fs	Plasma channel length	$\approx 200 \mu m$
Laser energy	$<$ 120mj	Plasma channel diameter	20-30μm
Optics numeric aperture	f/6	Max. el. energy (cut off)	10MeV (t.b.c)
Calc. focal spot radius	3μm	Electron energy peak @	5-6MeV
Calc. depth of focus	24μm	e-beam divergence (He)	$<$ 3deg
Meas. focal spot diam.	10μm	e-beam reproducibilty	poor (t.b.c)
		e-beam divergence (N)	$\approx$ 10deg
		e-beam reproducibility	good
		Bunch charge (N)	$>$ 0.1nC

References

[1] T.Tajima and J.M.Dawson. Laser electron accelerator. *Physical Review Letters*, 43(4):267, July 1979.

[2] J. Faure, Y. Glinec, and A. Pukhov et al. A laser–plasma accelerator producing monoenergetic electron beams. *Letters to Nature*, 431:541, September 2004.

[3] V. Malka, J. Faure, , and Y. Glinec et al. Monoenergetic electron beam optimization in the bubble regime. *Phys.Plasmas*, 12:056702, January 2005.

[4] J.Faure, Y.Glinec, and G.Gallot et al. Ultrashort laser pulses and ultrashort electron bunches generated in relativistic laser-plasma interaction. *Phys.Plasmas*, 13:056706, February 2006.

[5] A.Pukhov, S.Kilesev, and I.Kostyukhov et al. Relativistic laser plasma bubbles: new sources of energetic particles and x-rays. *Nucl.Fusion*, 44:S191–S201, December 2004.

[6] A.Pukhov, S.Gordienko, and S.Kilesev et al. The bubble regime of laser-plasma acceleration: monoenergetic electrons and the scalability. *Plasma Phys. Control. Fusion*, 46:B179–B186, 2004.

[7] I.Kostyukhov, A.Pukhov, and S.Kilesev. Phenomenological theory of laser-plasma interaction in "bubble" regime. *Phys.Plasmas*, 11(11):5256, November 2004.

[8] D. F. Gordon, R. F. Hubbard, and J. H. Cooley et al. Quasimonoenergetic electrons from unphased injection into channel guided laser wakefield accelerators. *Physical Review E*, page 026404, February 2005.

[9] D. Kaganovich, D. F. Gordon, and A. Ting. Observation of large-angle quasimonoenergetic electrons from a laser wakefield. *Phys.Rev.Lett*, 100:215002, May 2008.

[10] M.Galimberti. Realizzazione di un autocorrelatore a singolo impulso a dye. Technical Report 1/122002, IPCF-CNR Pisa, Dicember 2002.

[11] L.A.Gizzi, D.Giulietti, and A.Giulietti et al. Characterization of laser plasmas for interaction studies. *Phys.Rev.E*, 49(6):5628, June 1994.

[12] P.Tomassini and A.Giulietti. A generalization of abel inversion to non-axisymmetric density distribution. *Optics Communications*, 199:143–148, November 2001.

[13] Paolo Tomassini, Antonio Giulietti, and Leonida A. Gizzi et al. Analyzing laser plasma interferograms with a continuous wavelet transform ridge extraction technique: the method. *Appl.Opt.*, 40(35):6561, December 2001.

[14] F.Vittori. Analisi dati con specmag. Technical report, IPCF-CNR Pisa, September 2008.

[15] Marco Galimberti, Antonio Giulietti, and Danilo Giulietti et al. Sheeba: A spatial high energy electron beam analyzer. *Rev.Sci.Inst.*, 76:053303, April 2005.

[16] S.Agostinelli et al. GEANT4-a simulation toolkit. *NUCLEAR INSTRUMENTS & METHODS IN PHYSICS RESEARCH SECTION A-ACCELERATORS SPECTROMETERS DETECTORS AND ASSOCIATED EQUIPMENT*, 506(3):250–303, JUL 1 2003.

[17] L.A. Gizzi, A. Bacci, and S. Betti et al. An integrated approach to ultraintense laser sciences: the plasmon-x project. accepted for publication on Europ. Phys. Journal - Special Topics.